

## Extrusion nozzle design and print parameter selections for 3D concrete printing



Nan Zhang <sup>a,b,\*</sup>, Jay Sanjayan <sup>a</sup>

<sup>a</sup> Centre for Sustainable Infrastructure and Digital Construction, School of Engineering, Swinburne University of Technology, Hawthorn, Victoria, 3122, Australia

<sup>b</sup> Technical Centre of China State Construction Engineering Corporation, Beijing, 101300, China

### ARTICLE INFO

**Keywords:**

3D concrete printing  
Extrusion  
Printing quality  
Nozzle dimensions  
Print parameters

### ABSTRACT

3D concrete printing is a rapidly emerging technology. This study presents theoretical formulations for concrete extrusion resistance as a function of nozzle parameters. Results show that the extrusion resistances are related to the extrusion velocity of concrete and the cone angle and length of the nozzle. Lowering the extrusion velocity and nozzle length can reduce the extrusion resistance in the nozzle. Based on the results, a nozzle was customized to investigate the effects of print parameters, namely, printing speed (50–200 mm/s), printing height (5–40 mm), and extrusion velocity (96–288 mm/s), on printing quality. The reduction of printing speed increased the limits of layer thickness. Finally, the relationship among nozzle dimensions, print parameters, and filament dimensions was found, which can be used to pre-estimate the printing quality before printing and help preset appropriate printing parameters.

### 1. Introduction

3D concrete printing (3DCP) is one of the most promising approaches to promoting digital evolution in the construction industry, and it has been considerably advanced in the last few years [1–5]. Until now, 3DCP has evolved towards four main techniques: The most attractive one is extrusion-based 3D printing, which was pioneered by Khoshnevis et al. [6]. The idea is to use a robot to deposit concrete layer by layer. Another technique is called particle-based 3D printing, which uses binder liquid to selectively deposit into a powder (or aggregates) bed to bond the particles. Then, these unbound particles are cleared away [3,7]. The third one is named Digital Casting System which ETH Zurich initially developed. In this method, the concrete with a short setting time is cast into weak formworks [8] or a moving mold produced by the slip-forming method [9]. Besides, Technische Universität Braunschweig developed a Shotcrete 3D Printing (SC3DP) [10,11], which sprays the accelerated concrete to build up by controlling the compressed air in the printhead nozzle [12]. Among these, the extrusion-based 3D printing technique is considered the most potential for large-scale structures and has started to be applied in real construction projects [13]. Fig. 1 shows some recent projects completed using this printing technique.

Regarding the extrusion-based 3D printing technique, previous

studies reported the mixture design [14–16], extrudability [17–19], buildability and hardened properties [20–25] of printable concrete, which advances this technology. However, the control of printing quality in operation still faces challenges. As observed in Fig. 1, the surface of these printed buildings is inconsistent. In practice, the shaping of filaments is unpredictable before conducting empirical trials or adjusting print parameters while printing, which causes difficulty in controlling the printing quality. An acceptable printing quality means that these extruded filaments must be free of discontinuous surface defects resulting from excessive extrusion or inadequate cohesion. Furthermore, the layer edges must satisfy the dimension consistency [32]. To effortlessly extrude filaments with neat surfaces, some studies [6,14,20,33–35] used rectangular nozzles, even collaborating with trowels (in Fig. 2), instead of the circular one, but even so, the poor printing quality could still be unavoidable, as seen in Fig. 3. On the other hand, if the printing quality can be controlled well, the circular nozzle indeed has the potential to print freeform patterns. Fig. 4 exhibits some complex geometries accomplished using circular nozzles, but this is impossible (or difficult) for rectangular ones. Therefore, the control of printing quality for fresh concrete is essential for the extrusion-based printing technique.

It is well known that the printing quality is dominated by the print

\* Corresponding author. Centre for Sustainable Infrastructure and Digital Construction, School of Engineering, Swinburne University of Technology, Hawthorn, Victoria, 3122, Australia.

E-mail address: [nanzhang@swin.edu.au](mailto:nanzhang@swin.edu.au) (N. Zhang).



**Fig. 1.** a–f. 3D printed projects based on the extrusion-based 3D printing technique. (a) House Zero in USA (2022) [26], (b) Humanity Central in USA (2021) [27], (c) Holstebro House in Denmark (2021) [28], (d) Serendix in Japan (2022) [29], (e) Beckum House in Germany (2021) [30], and (f) Milestone House in Netherlands (2020) [31].

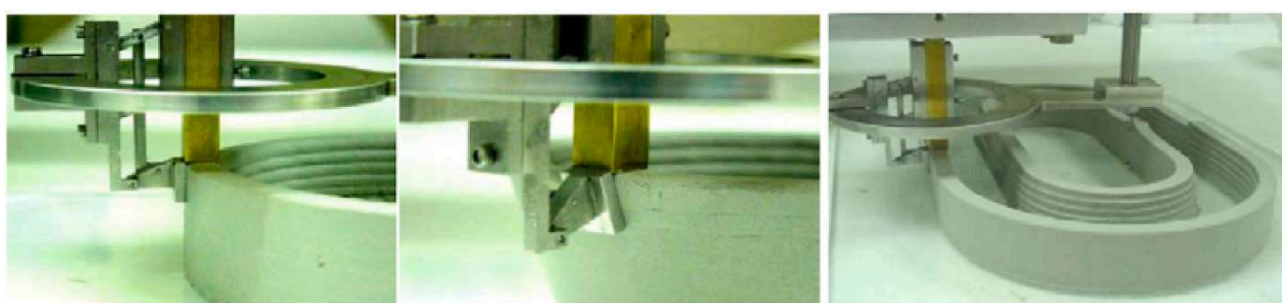


**Fig. 2.** Contour crafting with a controlled trowel by Khoshnevis [6].

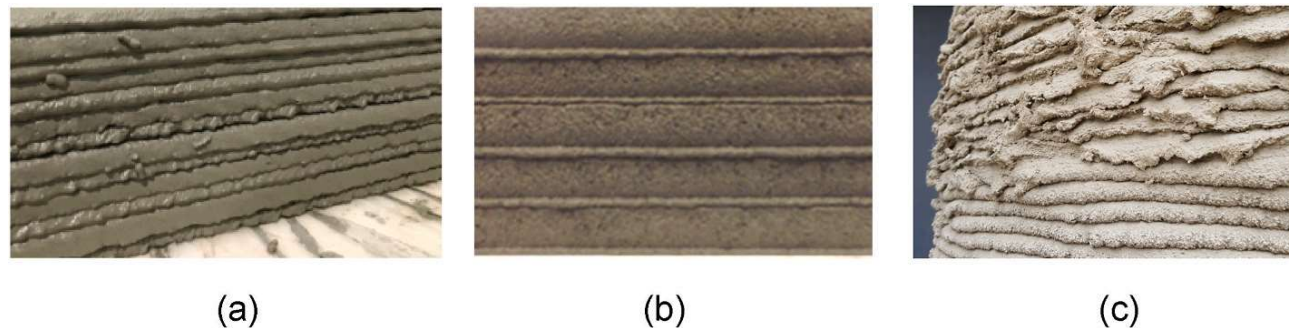


**Fig. 3.** Rough filaments extruded by (a) a rectangular nozzle without trowels [33] or (b) with trowels [34], and (c) a circular one without trowels.



**Fig. 4.** Printed products exhibiting attractive surfaces [36,37].

**Table 1**

Print parameters and nozzle features employed in the existing literature.

Research	Nozzle orifice shape	Nozzle size (mm)	Extrusion velocity (L/min)	Printing speed (mm/s)	Nozzle lift height (mm)
Rahul et al. [14]	Rectangular	30 × 20	1.6	44	20
Paul et al. [33]	Rectangular	10 × 20	3	150	–
Panda et al. [19]	Circular	10	0.5	80	–
Le et al. [38]	Circular	9	–	–	6
Asprone et al. [39]	Circular	25	–	20	20
Kazemian et al. [34]	Slice	–	–	60	25.4–38.1

parameters, including the printing speed, printing height, and extrusion velocity. The extrusion velocity is defined the flow velocity of concrete at the nozzle outlet, and the printing speed is the speed of the nozzle. Thus, the relationship among these parameters becomes critical for printing quality control. Table 1 summarizes these parameters employed in previous studies [14,19,33,34,38,39]. These parameters had a wide diversity as there has not been a general standard to guide the print parameter setup with different types of printable materials. Few studies have discussed the effect of print parameters on printing quality. For example, Panda et al. [40] showed a reduction in the layer width by increasing the printing speed under a fixed extrusion velocity. Tay et al. [41] found a significant effect of printing speed on the ratio between actual and expected filament sizes. However, there is limited literature reporting the correlation between nozzle features and print parameters and their effect on printing quality.

Besides, the extrusion resistance also influences the printing quality. Because printable concrete exhibits high yield stress and short setting time to meet requirements of buildability [17,42], the material without

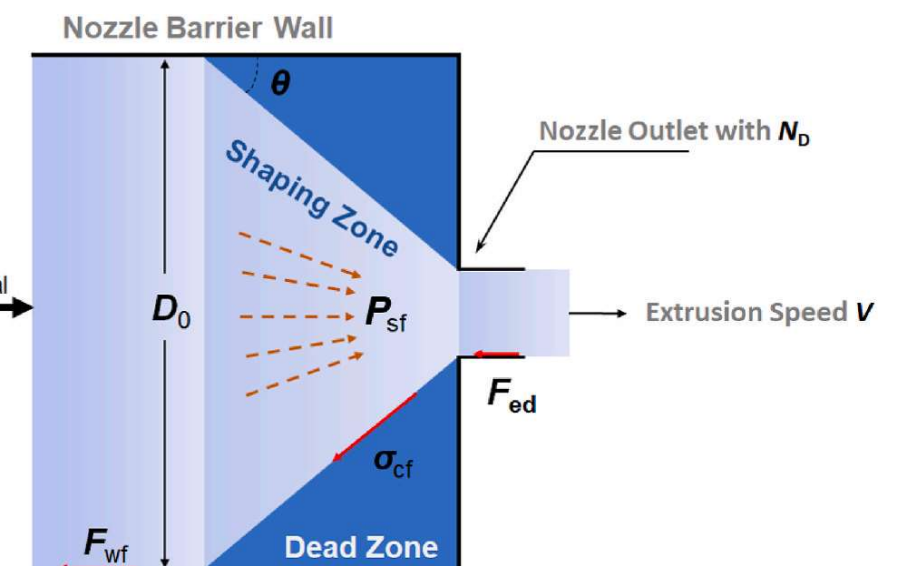


**Fig. 5.** Schematic illustration of the resistances acting on the fluid flowing in a nozzle.

flow is prone to remain stagnant and form the dead zone in the nozzle and delivery channels. The high yield stress could further result in high extrusion resistance in the nozzle [43], which will increase the possibility of blockages and cause discontinuous printing or even abortion. Thus, the nozzle must be designed to reduce the extrusion resistance for good printing quality.

To understand these factors affecting printing quality, this study first analyzes the extrusion resistance in a circular nozzle. Based on these theories, a printhead is designed by calculating the main extrusion resistances. Then, the customized printhead is used to investigate the effect of print parameters and nozzle dimensions on printing quality. Finally, the correlation among these parameters is attempted to obtain to achieve a good printing quality.

## 2. Theoretical formulation of extrusion process

In terms of fluid through a nozzle, the extrusion resistance should include four aspects. The first one is the wall friction force  $F_{wf}$  against the

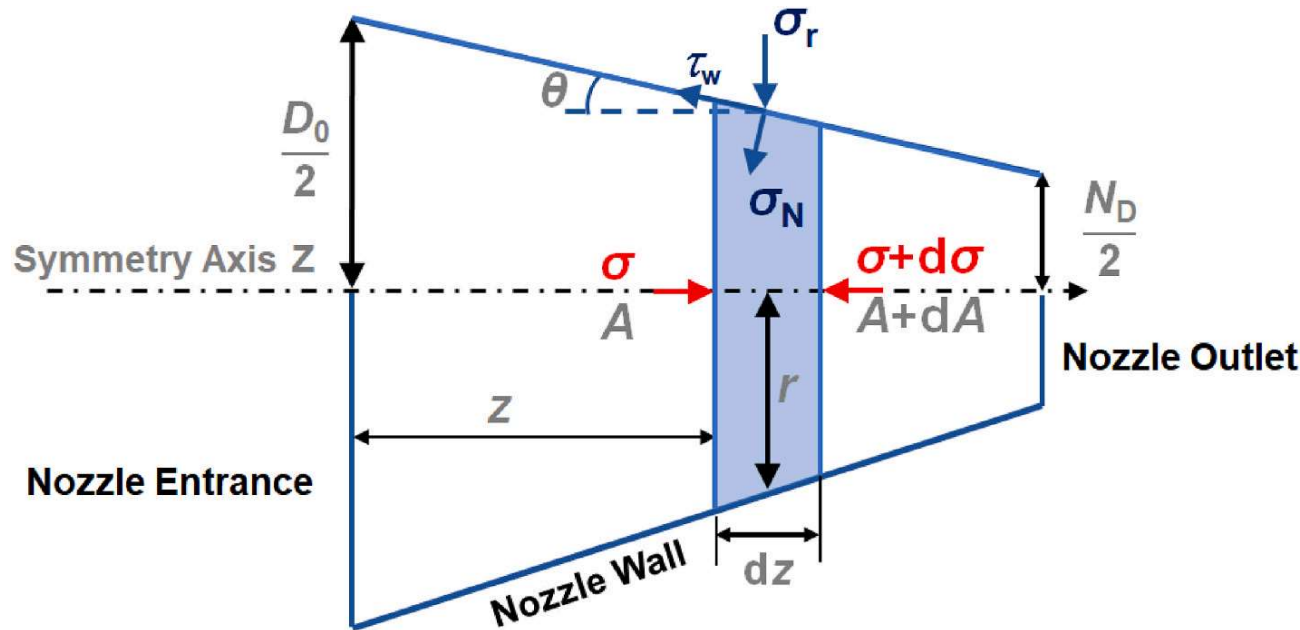


Fig. 6. Forces acting on an infinitesimally thin element in a nozzle cone.

flow direction [44]. Its value depends on the length of the nozzle and the roughness of the inner wall. If the nozzle outlet has an extra die, there will exist an additional friction force  $F_{ed}$  acting on the inner surface of the die [44,45]. Besides, when the fluid flows through the outlet, the dead zone will form near the outlet, followed by the presence of two resistances, such as the shaping pressure  $P_{sf}$  and the conical friction stress  $\sigma_{cf}$ . They are associated with the cone angle  $\theta$  of the dead zone [46, 47]. Fig. 5 presents the four resistances acting on the fluid flowing through a nozzle with a die. Thus, in terms of extruding printable concrete, the lengths of the nozzle barrier wall and the extra die should be as short as possible against high wall friction force.

The shaping pressure  $P_{sf}$  pushes the fluid into the shaping zone (in Fig. 5), where the flow lines of the fluid converge towards the nozzle outlet [43,48]. According to Basterfield et al.,  $P_{sf}$  can be expressed by Ref. [43]:

$$P_{sf} = \sqrt{3}\tau_d \ln \frac{D_0}{N_D} + \frac{\mu\sqrt{3}^{n+1}}{2^n \cdot 3^n} \left( \frac{2V}{N_D} \right)^n \times [\sin \theta (1 + \cos \theta)]^n \cdot \left[ 1 - \left( \frac{N_D}{D_0} \right)^{3n} \right] \quad (1)$$

where  $V$  is the average extrusion velocity,  $\tau_d$  is the dynamic yield stress,  $\mu$  is the plastic viscosity,  $n$  is the flow index,  $D_0$  and  $N_D$  are the entrance and outlet diameters of the nozzle, respectively. It can be known from Eq. (1) that when the dynamic yield stress and plastic viscosity are given,  $P_{sf}$  is mainly related to the nozzle dimensions and the extrusion velocity.

Apart from that, the flow could suffer from the conical friction stress  $\sigma_{cf}$  on the interface between the shaping zone and the dead zone, as shown in Fig. 6. According to Khelifi [44], the conical friction stress can convert to an axial resistance, which is denoted by  $\sigma_{ac}$ . To calculate this resistance, the flow rate is assumed as zero in the dead zone and the zone shape is a nearly conical exit geometry at an angle  $\theta$  to the symmetry axis of the nozzle orifice [43,49–51]. Moreover, the distance from the nozzle entrance to a position on the symmetry Z-axis is denoted by  $z$ . Hence, these stresses acting on the cylindrical element at the  $z$  position can be presented in Fig. 6 [44], where  $dz$  is the thickness of the element,  $D_0$  and  $N_D$  are the nozzle entrance and outlet diameters,  $\sigma$  and  $(\sigma + d\sigma)$  are the axial pressures on both sides of the element, and  $\sigma_N$  is the normal stress acting on the nozzle's inner surface. Furthermore, the radial stress  $\sigma_r$  acting on the nozzle wall is perpendicular to the symmetry centerline of the conical nozzle and it depends on both the axial pressure  $\sigma$  and the internal friction angle  $\varphi$  of the fluid as follows [44]:

$$\sigma_r = (1 - \sin \varphi) \bullet \sigma \quad (2)$$

Based on this model, it can be known that when the cone angle of the nozzle is smaller than the  $\theta$  of the dead zone, the dead zones will disappear. In that case, the material around the nozzle wall will be

directly sheared on the nozzle wall rather than with the material of the dead zone. Therefore,  $\tau_w$  in Fig. 6 should be equal to the wall shear stress. In addition, the wall shear stress is taken as a fraction of the internal shear stress [44]. This study assumed the ratio as 0.65 in accordance with Khelifi et al. [44], so the wall shear stress  $\tau_w$  can be expressed as a simple Coulomb law:

$$0.65 \tau_w = (C + \sigma_N \tan \varphi) \quad (3)$$

where  $C$  is the yield stress of the fluid [44]. According to Lu and Wang [52], the value of  $C$  can be equivalent to the static yield stress  $\tau_s$  as the flow velocity around the nozzle wall is close to zero. Eq. (3) can thus be rewritten by:

$$0.65 \tau_w = (\tau_s + \sigma_N \tan \varphi) \quad (4)$$

If the cone angle of the nozzle is equal to  $\theta$  without dead zones, there is a balance among these stresses on the Z-axis, as presented by Eq. (5). The left side represents the pressure acting on the nozzle entrance minus the wall resistance, and the right side denotes the pressure on the nozzle outlet.

$$\sigma A - \left( \sigma_N 2\pi r \frac{dz}{\cos \theta} \right) \sin \theta - \left( \tau_w 2\pi r \frac{dz}{\cos \theta} \right) \cos \theta = (\sigma + d\sigma)(A + dA) \quad (5)$$

Furthermore, the radial stress  $\sigma_r$  can be given by:

$$\sigma_r = \sigma_N \cos \theta - \tau_w \sin \theta \quad (6)$$

and the cross-sectional area is expressed by:

$$A = \pi r^2 = \pi \left( -\tan \theta \bullet z + \frac{D_0}{2} \right)^2 \quad (7)$$

Substituting Eqs. (2), (4), (6) and (7) into Eq. (5) yields:

$$\frac{d\sigma}{dr} = \frac{2}{r} \left\{ \sigma \left[ \frac{(1 - \sin \varphi)(0.65 \tan \theta + \tan \varphi)}{0.65 \sin \theta - \tan \varphi \sin \theta \tan \theta} - 1 \right] + \frac{\tau_s}{0.65 \sin \theta \cos \theta - \tan \varphi \sin \theta^2} \right\} \quad (8)$$

By integrating Eq. (8) between  $r = D_0/2$  and  $N_D/2$ , the axial resistance  $\sigma_{ac}$  can be obtained as follows:

$$\sigma_{ac} = \frac{K_2}{K_1} \left[ \left( \frac{D_0}{N_D} \right)^{2K_1} - 1 \right] \quad (9)$$

where  $K_1$  and  $K_2$  are both constant:

$$K_1 = \frac{(1 - \sin \varphi)(0.65 \tan \theta + \tan \varphi)}{0.65 \sin \theta - \tan \varphi \sin \theta \tan \theta} - 1 \quad (10)$$

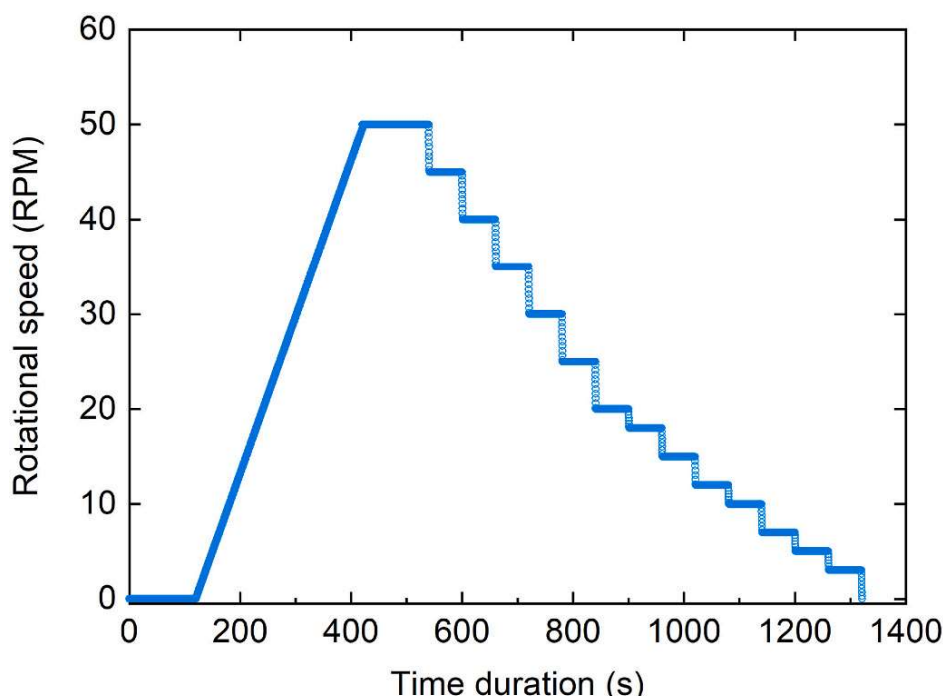
$$K_2 = \frac{1}{0.65 \sin \theta \cos \theta - \tan \varphi \sin \theta^2} \quad (11)$$

**Table 2**

Mix proportions of the reference concrete.

Cement	Sand	Water	HRWRA (%)	REA (%)	VMA (%)
1.0	1.0	0.37	0.1	0.2	2.2

Note: All numbers are weight ratios of the cement weight of 1.

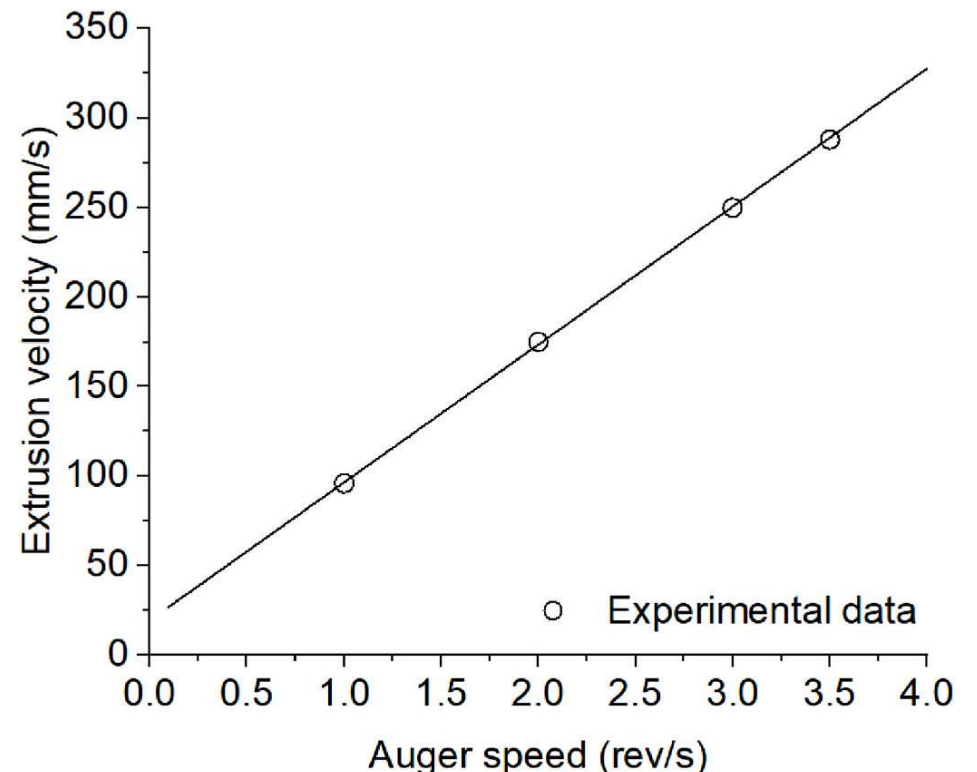
**Fig. 7.** The gantry system used in this study.**Fig. 8.** Experimental data of rotational speed as a function of time.

It can be known from Eq. (9) that for constant rheological behaviors,  $\sigma_{ac}$  is only related to the nozzle dimensions.

### 3. Materials and experimental methods

#### 3.1. Mix proportion

A commercial Portland Cement (CEM II 42.5 N), complying with BS EN 197-1:2011 [53], and silica sand with a nominal maximum size of 4 mm were used. The reference mixture needs to primarily meet the extrudability of printable concrete [38] while providing sufficiently long open time for stable rheology properties during testing. After a series of trials, the mix proportion was determined as presented in Table 2. A polycarboxylate-based high-range water-reducing agent (HRWRA), a commercially available viscosity modifying agent (VMA) and a sodium gluconate retarder (REA) were used to adjust the workability and open time of the concrete. The difference between the spread diameters measured in 2 h was close to zero.

**Fig. 9.** Extrusion velocity versus auger speed.

#### 3.2. Print equipment

The customized printhead was employed in the print system (Fig. 7). This printer utilizes a gantry system to control the path of the auger-type printhead across the print platform, which is 2800 mm in length, 1500 mm in width and 1800 mm in height. The printhead has a round nozzle with a 24-mm outlet diameter, as illustrated in Fig. 8. The fresh concrete was first mixed in a 50-L concrete mixer and then delivered through a concrete screw pump into the printhead.

#### 3.3. Experimental methods

##### 3.3.1. Rheological behaviors

The static and dynamic yield stresses and plastic viscosity of the concrete were evaluated using a coaxial cylinder rheometer (Viskomat XL [54]) with a cage and a six-blade vane probe. The probe diameter and height are both 69 mm. The gap from the probe to the cage is 40 mm, which is the same as the one from the probe bottom to the unit cell.

According to the definition of static yield stress [55], its value corresponds to the peak of shear stress before the material flows. In addition, a low rotational speed (or shear rate) is widely used to evaluate the static yield stress [14,56–58] since a high speed will overestimate the static yield stress [14]. In this study, the rotational speed to measure the static yield stress was controlled at a slow rate of 2.5°/min for 2 min, and then it was accelerated to 50 RPM. After remaining for 2 min, the speed was reduced at spaced steps, each step lasting 1 min. Fig. 8 shows the testing procedure of the rotational speed versus time.

##### 3.3.2. Extrusion velocity

To evaluate the extrusion velocity, the amount of concrete extruded from the nozzle unit time was measured by controlling the rotational speed of the auger at 1, 2, 3, and 3.5 rev/s. As this auger needs about 1 s to accelerate to the target speed from zero, the extrusion flow unit time is uneven at the beginning of auger operation. To exclude this, the amounts (denoted by  $M_{5s}$  and  $M_{25s}$ ) of extruded concrete in 5 s and 25 s after operation were collected via an electronic scale with 0.01g precision. Also, the material attached to the nozzle outlet was contained. The extrusion velocity can thus be calculated by Eq. (12).

$$V = \frac{4(M_{25s} - M_{5s})}{\pi \rho t N_D^2} \quad (12)$$

where  $V$  is the extrusion velocity,  $t$  is the time difference of 20 s, and  $\rho$  is the concrete density of  $2200 \text{ kg/m}^3$ . As seen in Fig. 9, the extrusion

**Table 3**

Print parameters used in this study.

Name	Experimental value
Extrusion velocity $V$	96 mm/s, 175 mm/s, 250 mm/s, 288 mm/s
Printing speed $S_p$	50 mm/s, 100 mm/s, 150 mm/s, 200 mm/s
Nozzle lift height after printing each layer ( $H_{nl}$ in Fig. 18)	5 mm, 10 mm, 15 mm, 20 mm, 25 mm, 30 mm, 35 mm, 40 mm

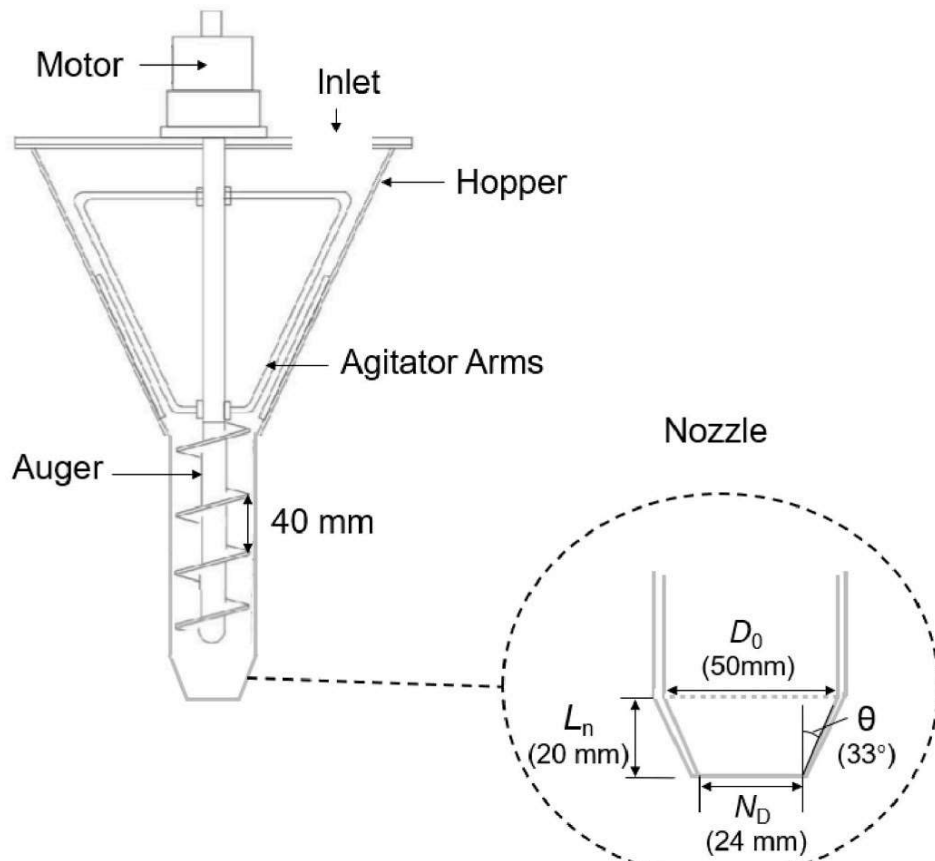


Fig. 10. Geometrical details of the customized printhead.

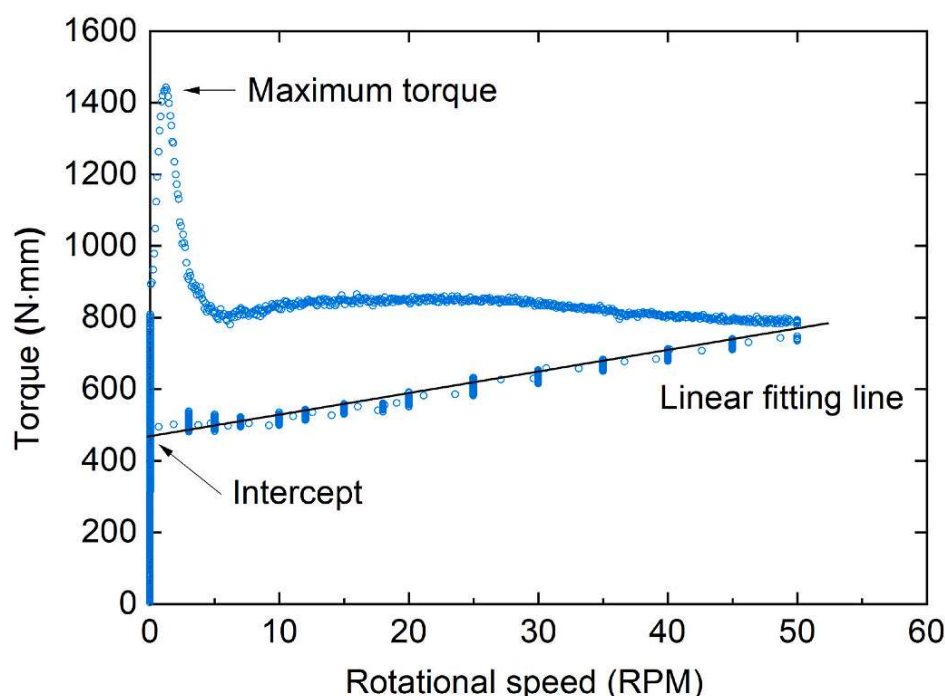


Fig. 11. Torque results as a function of the rotational speed.

velocity shows a linear relationship with the auger speed.

### 3.3.3. Filament dimensions

The testing of filament dimensions was executed at different print parameters in Table 3. First, three filaments with a length of 300 mm were extruded successfully in a vertical direction under the same print parameters. Afterwards, the width and height were measured at ten random positions of the filament except for the acceleration segment. Each test was repeated twice.

**Table 4**

Rheological properties of the reference printable concrete.

Static yield stress (Pa)	Dynamic yield stress (Pa)	Plastic viscosity (Pa·s)	Flow index
2823.5	432.2	45.3	1

## 4. Printhead design

To address the flow requirement of concrete during printing, the auger was customized with an outside diameter of about 50 mm and a screw pitch of 40 mm, so the nozzle entrance diameter  $D_0$  was set to 50 mm against dead zones in the nozzle barrier wall. The prototype of the printhead with a circular nozzle is shown in Fig. 10. The agitator's arms were fixed above the auger to scrape the stagnant concrete on the inner wall of the hopper. According to the extrusion resistance theory, the bottom of the auger was designed near the nozzle entrance, so the wall friction resistance in the nozzle can be eliminated. Also, the extra die was removed to avoid the additional friction force  $F_{ed}$ . Therefore, the extrusion resistances subjected in the nozzle should be dominated by the shaping pressure  $P_{sf}$  and the axial resistance  $\sigma_{ac}$ . To further reduce the mixing resistances, these rheological parameters, including static and dynamic yield stresses, plastic viscosity, and flow index, need to be measured to evaluate  $P_{sf}$  and  $\sigma_{ac}$  with different nozzle dimensions.

### 4.1. Measurement of rheological parameters

Fig. 11 shows the torque versus rotational speed using the coaxial cylinder rheometer. The ascending and descending curves presented hysteresis, which is due to the thixotropic behavior of printable concrete [42]. Furthermore, the torque in the downward curve linearly reduced with the decrease of the rotational speed. This is in agreement with a typical Bingham Plastic fluid, so the flow index  $n$  is equal to 1.

By measuring the upper-curve peak in the hysteresis loop, the static yield stress  $\tau_s$  was calculated by Eq. (13) [59].

$$\tau_s = \frac{T_{max}}{2\pi R_i^2 h} \quad (13)$$

where  $h$  is the height of the inner cylinder submerged in concrete in coaxial cylinders rheometer,  $T_{max}$  is the maximum torque, and  $R_i$  is the inner cylinder radius of the coaxial cylinder rheometer. Besides, the dynamic yield stress  $\tau_d$  and the plastic viscosity  $\mu$  were calculated by Eq. (14) [59]:

$$\begin{aligned} \tau_d &= \frac{\left(\frac{1}{R_i^2} - \frac{1}{R_o^2}\right)}{4\pi h \ln\left(\frac{R_o}{R_i}\right)} G \\ \text{and} \\ \mu &= \frac{\left(\frac{1}{R_i^2} - \frac{1}{R_o^2}\right)}{8\pi^2 h} H \end{aligned} \quad (14)$$

where  $G$  and  $H$  are the intercept and inclination of the fitting line to the descending curve in Fig. 11, and  $R_o$  is the outer cylinder radius of the rheometer. Table 4 summarized the rheological parameters.

Besides, according to previous studies [18,20], the friction angle  $\varphi$  is assumed as 20°. Next, the rheological parameters will be used to determine the rest of nozzle dimensions.

### 4.2. Nozzle design

The shaping pressure  $P_{sf}$  was calculated by Eq. (1) and is shown in Fig. 12. It can be found that the  $P_{sf}$  increases with the increases of the nozzle cone angle  $\theta$  and the extrusion velocity  $V$ . Moreover, these increments become obvious by increasing the nozzle length  $L_n$ . For

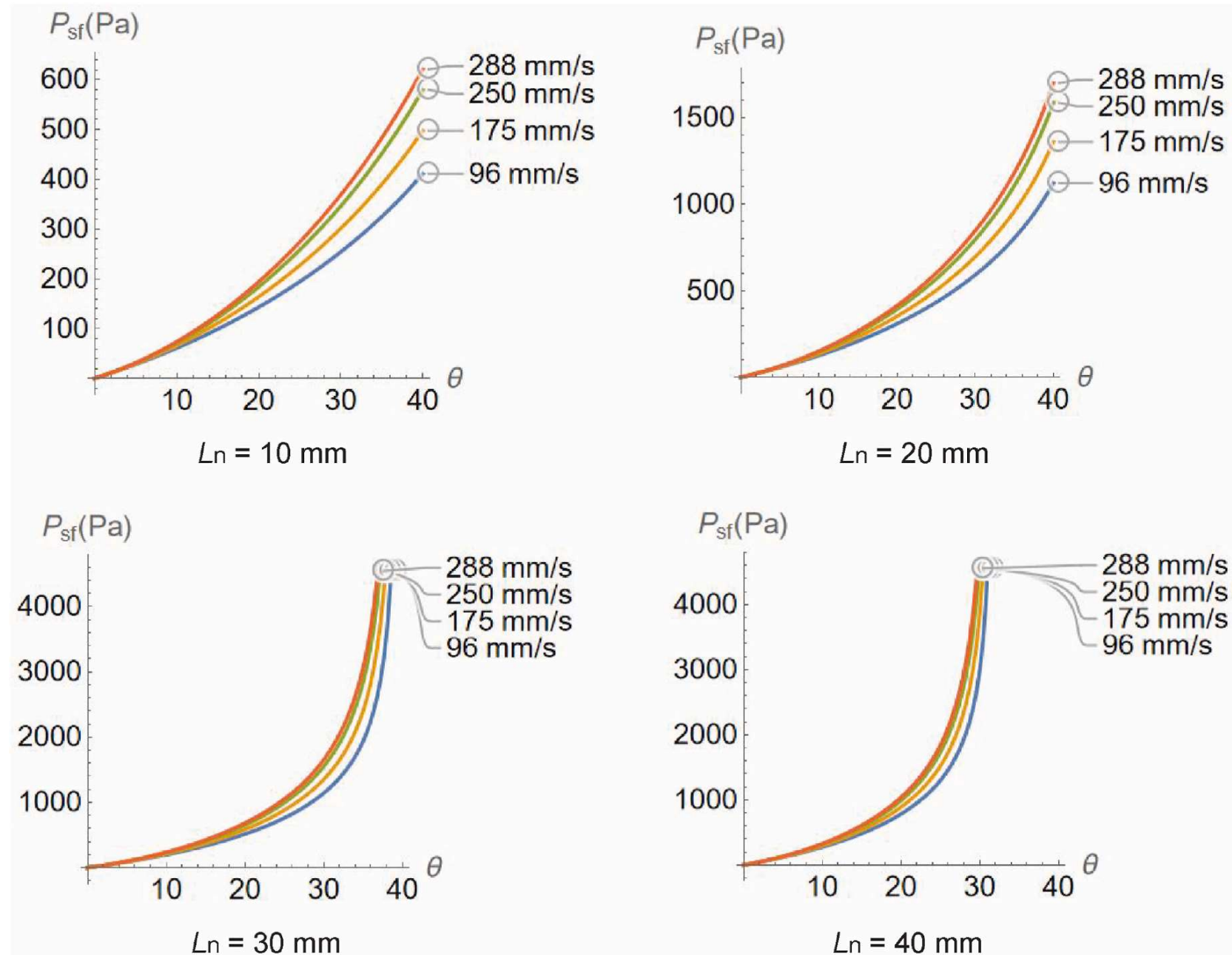


**Fig. 12.** The shaping pressure  $P_{sf}$  as a function of the cone angle  $\theta$  and nozzle length  $L_n$  at different extrusion velocities.

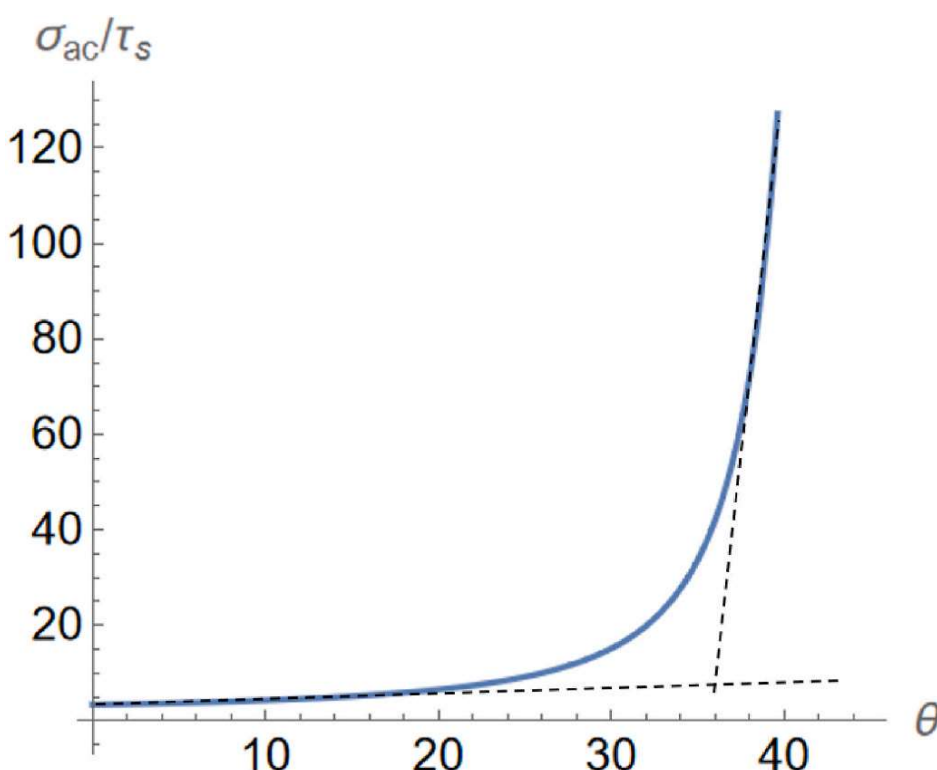


**Fig. 13.** Dimensionless axial resistance caused by the conical friction as a function of the cone angle  $\theta$ .

example, for a nozzle length of 30 mm, the  $P_{sf}$  is around 1000 Pa at  $\theta$  of 25° and it surges to more than 4000 Pa at  $\theta$  of 40°. When the nozzle length extends to 40 mm, the surge appears at  $\theta$  of 20°. Thus, the increase of the nozzle length narrows the range of  $\theta$  in which the shaping pressure acting on the fluid can remain low. As the  $\theta$  dominates the nozzle outlet diameter, the nozzle length is expected to be short for a

**Table 5**  
The calculated extrusion resistances at different extrusion velocities.

Extrusion resistance	Extrusion velocity			
	96 mm/s	175 mm/s	250 mm/s	288 mm/s
$\sigma_{ac}$ (kPa)	65.6	65.6	65.6	65.6
$P_{sf}$ (Pa)	710.8	843.5	969.6	1033.4

wide range of the nozzle outlet with a low shaping pressure. On the other hand, if the nozzle is too short, the nozzle outlet is close to the bottom of the auger. The very short extrusion process would result in low compaction of extruded filaments. Moreover, Domanti and Bridgwater [60] found that the short extrusion channel would cause surface fractures. Therefore, the nozzle length  $L_n$  was set to 20 mm, in which  $P_{sf}$  is low in a wide range of  $\theta$  up to 40°.

Next, the axial resistance  $\sigma_{ac}$  was calculated by Eq. (9) with  $L_n = 20$  mm and  $D_0 = 50$  mm. Fig. 13 shows the dimensionless axial stress ( $\sigma_{ac}/\tau_w$ ) versus the cone angle  $\theta$ . It can be seen that the value surges at  $\theta$  of 40°. Considering a fall of concrete caused by self-weight, this study designed the  $\theta$  around 33°. Afterwards, the outlet diameter  $N_D$  of the nozzle was set to 24.0 mm in accordance with Eq. (15).

$$N_D = D_0 - 2L_n \tan \theta \quad (15)$$

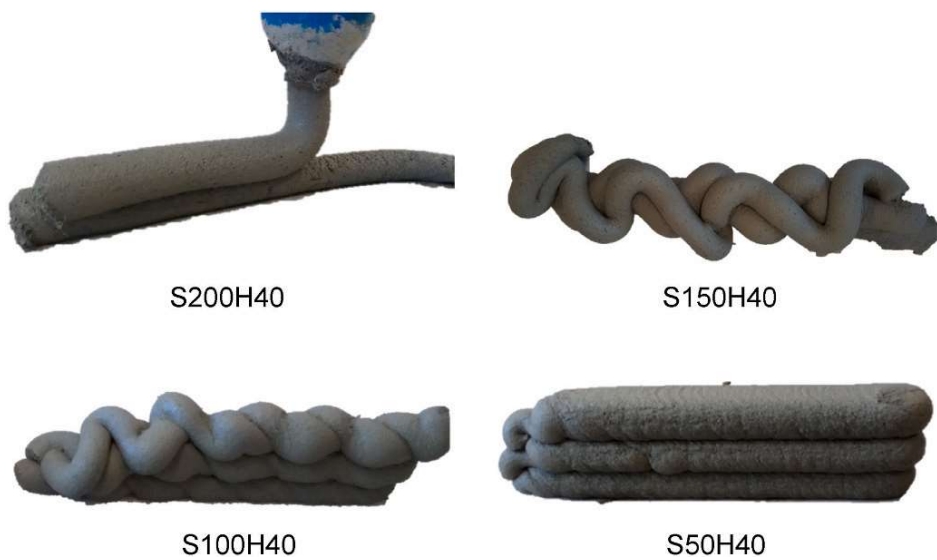
Based on these given dimensions of the nozzle, the shaping pressure  $P_{sf}$  and the axial resistance  $\sigma_{ac}$  of the customized nozzle can be calculated. Table 5 summarizes these extrusion resistances at different extrusion velocities.

It is clear that  $\sigma_{ac}$  caused by the conical friction is much higher than  $P_{sf}$ . This is because the former is dominated by the static yield stress

**Table 6**

Print parameters of these filaments.

NO.	Extrusion velocity (mm/s)	Nozzle lift height (mm)	Printing speeds (mm/s)
S50H40	175	40	50
S100H40	175	40	100
S150H40	175	40	150
S200H40	175	40	200
S50H5	288	5	50
S200H5	288	5	200

**Fig. 14.** Filaments overlapped at different printing speeds with the extrusion velocity of 175 mm/s and the nozzle lift height of 40 mm.

whereas the latter is dependent on the dynamic yield stress. As presented in Table 4, the static yield stress was more than 6 times the dynamic yield stress due to the thixotropy of printable concrete. From this result, it can be known that reducing the yield stress of printed concrete can bring low extrusion resistances in the nozzle, but this reduction is indeed limited by addressing the buildability of concrete after extrusion. Therefore, for a given nozzle, lowering the extrusion velocity is an available approach to reducing the extrusion resistance.

## 5. Results and discussion

### 5.1. Layer shape

To evaluate the printing quality using the customized nozzle, the shape of these filaments extruded at different print parameters (in Table 6) were first observed.

Fig. 14 shows the shape of these filaments extruded at the extrusion velocity of 175 mm/s and the nozzle lift height of 40 mm. It can be seen that these filaments of S200H40 could not be overlapped in the vertical direction. It is because the nozzle lift height was much higher than the layer thickness that the printer can enable to achieve under the print

parameters. In that case, there was insufficient time to fill concrete into the expected dimension space. By reducing the printing speed, more material was filled into the space, but the layer shape was still random and dissatisfied the dimension consistency, such as S150H40 and S100H40. After the filament height reached the nozzle lift height, these filaments can exhibit uniform dimensions like S50H40 in Fig. 14. The same phenomenon can also be observed at different print parameters. This result indicates that there should be an upper limit in print parameters to satisfy good printing quality. When these parameters exceed the upper limit, the expected space unit time will not be filled, resulting in the fact that extruded filaments cannot be overlapped with uniform dimensions.

On the other hand, when the extrusion amount of concrete was more than the expected dimension space, part of the extruded concrete was squeezed into the overlapped filaments. As the nozzle outlet scraped on the top of the filament during printing, the layer thickness remained the nozzle lift height, but causing surplus blocks on both sides of filaments, such as S50H5 in Fig. 15. By increasing the printing speed, these surplus blocks can gradually disappear. For S200H5 at a printing speed of 200 mm/s, these filaments were uniform without any surplus blocks.

Therefore, it can be concluded that to achieve desired printing quality with good dimension consistency and free of surface defects, the nozzle lift height should be equal to the layer thickness. This was also found by this study [61]. Furthermore, these print parameters need to be controlled within certain limitations, which will be discussed next.

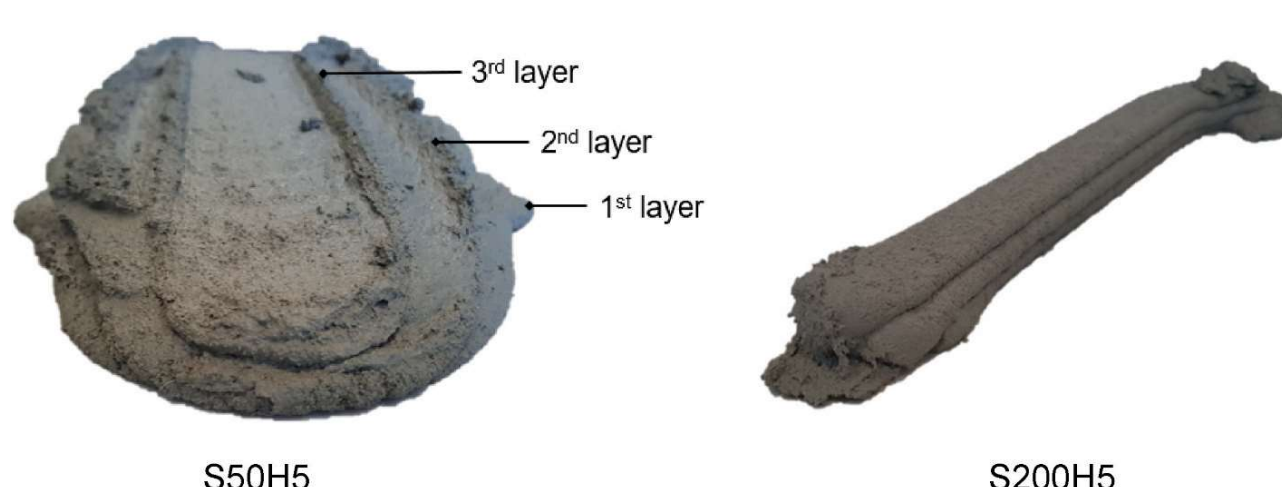
### 5.2. Layer dimensions

Fig. 16 shows the relationship between the extrusion velocity and the width of these filaments with the good printing quality. When the printing height was fixed, the layer width increased linearly with increasing extrusion velocity, regardless of printing speeds. However, the slope of the linear relationships varied at different printing speeds and printing heights.

Interestingly, the decrease in printing speed increased the limit of filament thickness. At the printing speed of 50 mm/s, the maximum and minimum values of filament thickness were 40 mm and 15 mm, and the height interval was 25 mm. When the printing speed increased to 200 mm/s, the maximum and minimum thicknesses reduced to 20 mm and 5 mm, in which the interval decreased to 15 mm. Furthermore, Fig. 16 shows that the lowest width of extruded filaments was always larger than the nozzle outlet diameter (24 mm), independent of print parameters. For the filaments narrower than 24 mm, their surfaces had discontinuous defects.

### 5.3. Relationship between print and nozzle parameters

To investigate the correlation among nozzle dimensions, print parameters and layer width, a formula is introduced as follows:

**Fig. 15.** Filaments extruded at two printing speeds with an extrusion velocity of 288 mm/s and a nozzle lift height of 5 mm.

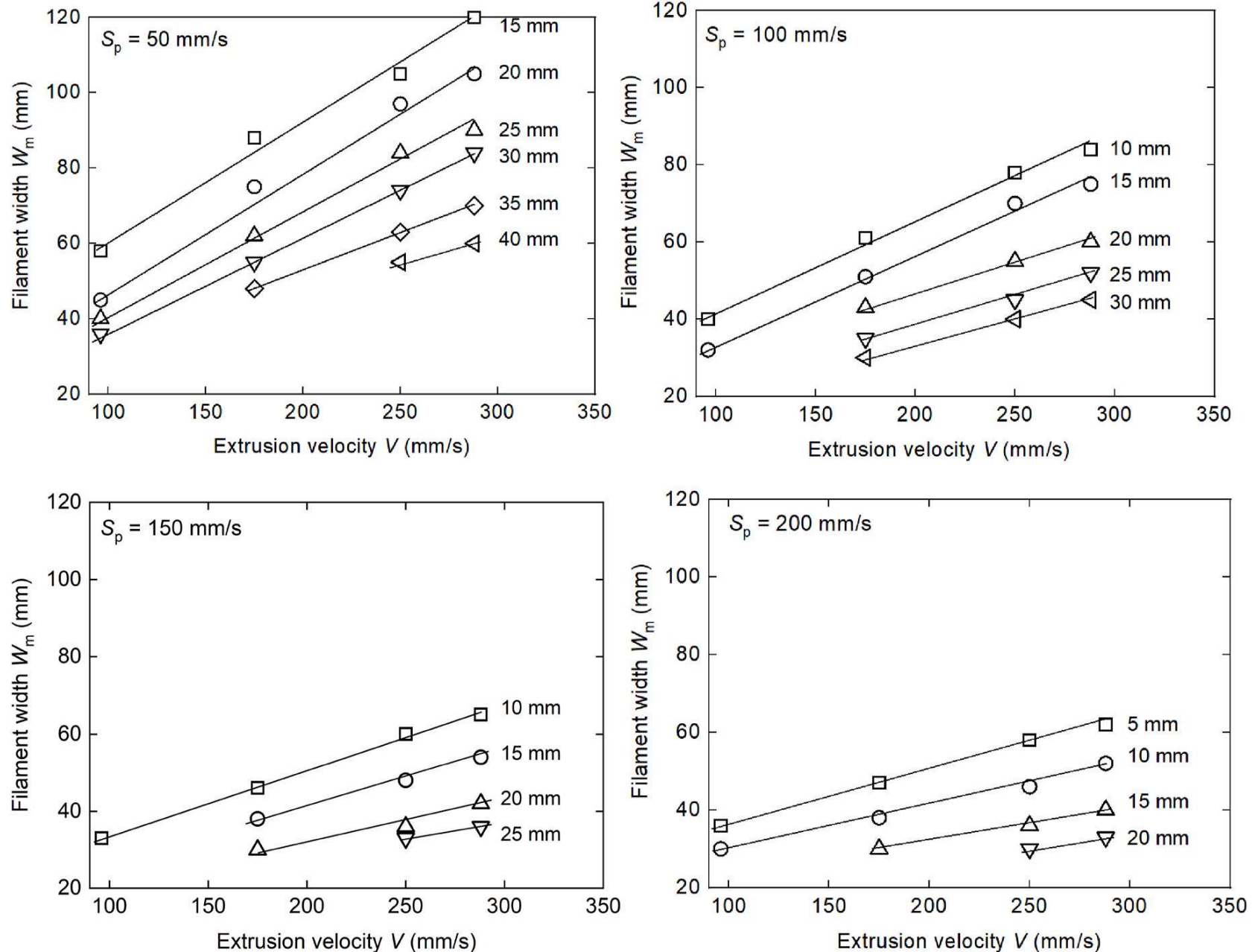


**Fig. 16.** Filament width as a function of extrusion velocity at different printing heights.

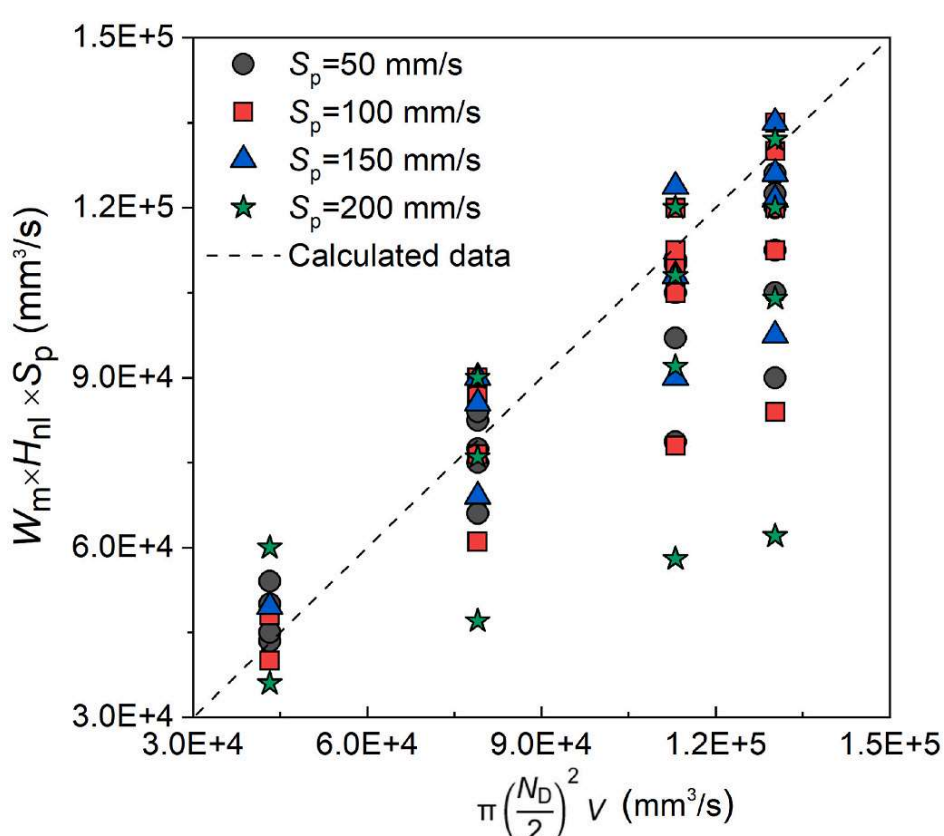


**Fig. 17.** The correlation among the nozzle outlet diameter, filament width and print parameters, including extrusion velocity, printing speed, and printing height.

$$W_m H_{nl} S_p = \pi \left( \frac{N_D}{2} \right)^2 V \quad (16)$$

However, the theoretical data showed an apparent difference from

the experimental data, as presented in Fig. 17.

To modify this formula, a theoretical upper surface is assumed for the extruded filament, as presented in Fig. 18. The distance between the theoretical surface and the practical surface (corresponding to the printing height \$H\_{nl}\$) is denoted by the absolute value of \$\kappa H\_{nl}\$. When the theoretical surface is below the level of \$H\_{nl}\$, the value of \$\kappa\$ is less than 0, as illustrated in Fig. 18(a). In this case, the cross-section of the filament cannot be filled by the material extruded unit time, which corresponds to S100H40 and S150H40 in Fig. 14. On the other hand, when the theoretical surface is higher than the \$H\_{nl}\$, the \$\kappa\$ is greater than 0 (Fig. 18(b)). For that case, as the nozzle bottom scrapes the filament's upper surface, the material within \$\kappa H\_{nl}\$ will be squeezed to both sides of the filaments like S50H5 in Fig. 15. Based on this assumption, Eq. (16) can be modified as follows:

$$W_m H_{nl} S_p = \pi \left( \frac{N_D}{2} \right)^2 V + \kappa H_{nl} (N_D - W_m) \quad (17)$$

In accordance with Eq. (17), the value of \$\kappa\$ can reflect the deviations between experimental and calculated data in Fig. 17. By taking experimental data into Eq. (17), the corresponding \$\kappa\$ can be obtained. To understand the limits of \$\kappa\$, two periods of time are introduced. One of them is denoted by \$t\_1\$ during which the nozzle moves a distance of \$N\_D\$ and it can be expressed by:

$$t_1 = \frac{N_D}{S_p} \quad (18)$$

The second one is denoted by \$t\_2\$ during which the concrete extruded from the nozzle outlet moves to the top surface of the overlapped filament, and can be written by:

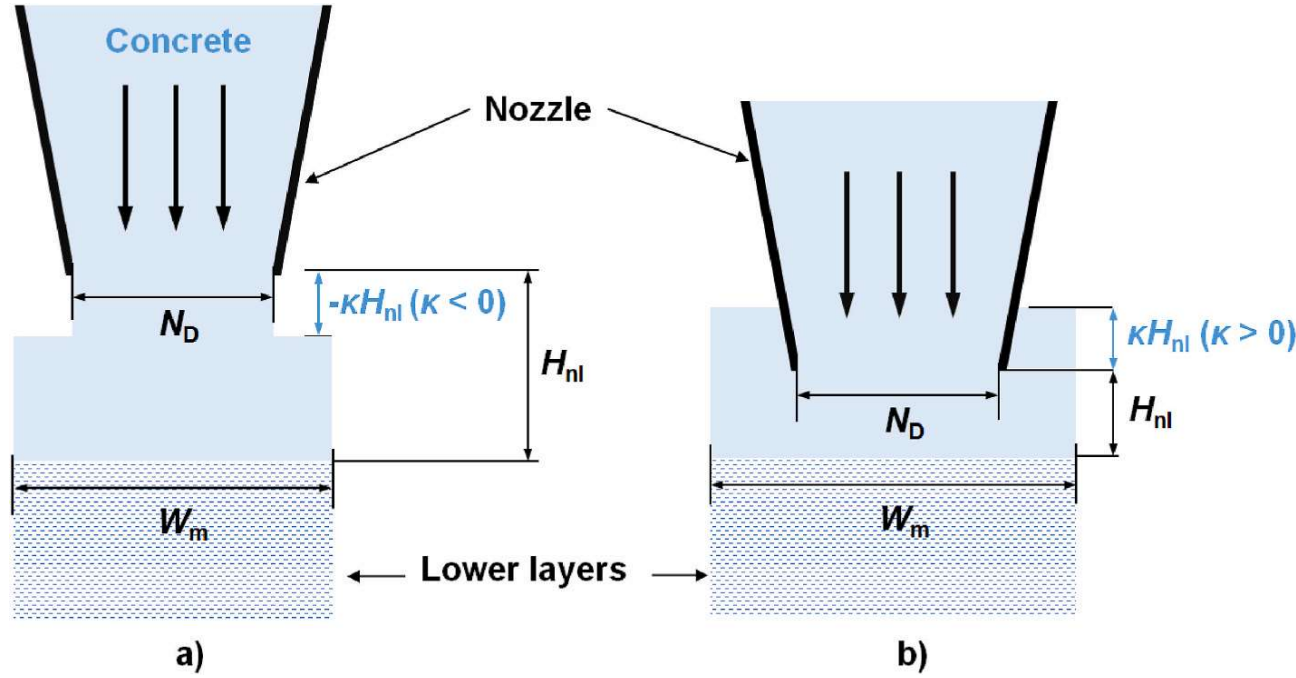
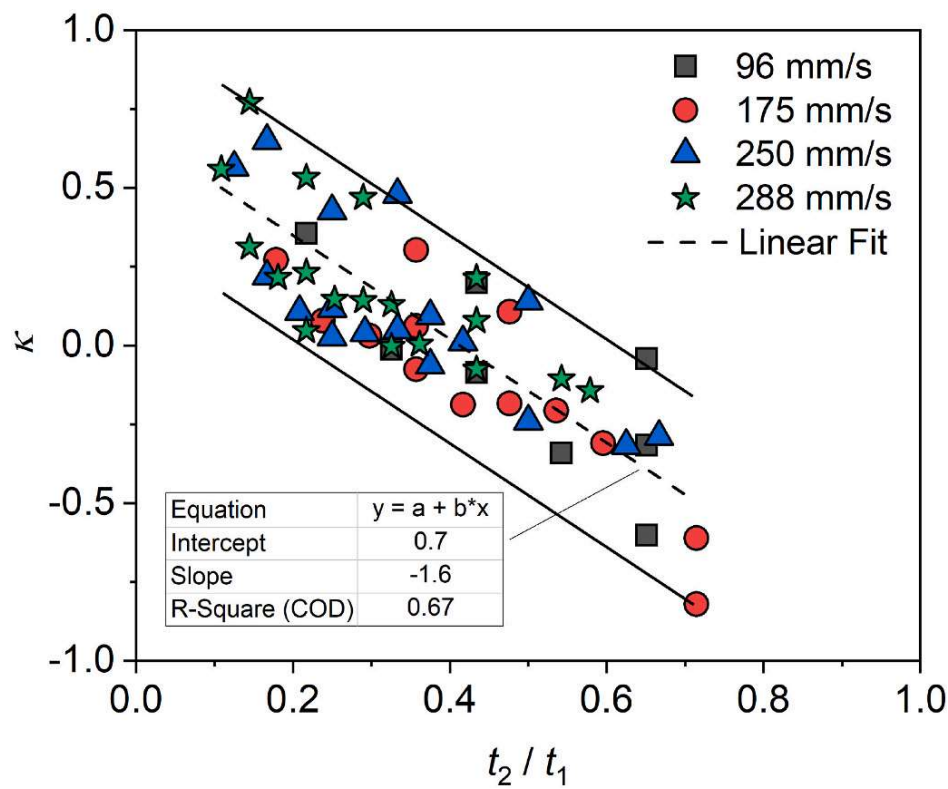


Fig. 18. The cross-section of a filament that is being extruded.

Fig. 19. Ratios of  $t_2$  to  $t_1$  as a function of  $\kappa$ .

$$t_2 = \frac{H_{nl}}{V} \quad (19)$$

Then, it is presumed that  $\kappa$  could be related to the proportion between  $t_1$  and  $t_2$ , and their relationship is plotted in Fig. 19.

Fig. 19 shows that the ratio of  $t_2$  to  $t_1$  was limited between 0.1 and 0.7. This coincides with the conclusion in Section 5.1. On the one hand, when the ratio is too high, the filament is elongated due to frictional resistance generated by touching the top surface of deposited layers. As a result, the length after deposition is longer than the original length of the fresh filament extruded from the nozzle without any external forces except gravity and extrusion force. This causes a narrower width than the nozzle outlet diameter. When the extrusion amount of material cannot be provided sufficiently, the filament will be discontinuous. On the other hand, when  $t_2 \ll t_1$ , the fresh filament extruded from the nozzle would be squeezed. In this case, the length after deposition is shorter than its original length, followed by a wider width than the nozzle diameter. It is known from Fig. 19 that the phenomenon occurred when the ratio of  $t_2$  to  $t_1$  was lower than 0.1. These findings are in agreement with those mentioned in Sections 5.1 and 5.2.

As shown in Fig. 19, all data of  $\kappa$  are distributed around the correlation as follows:

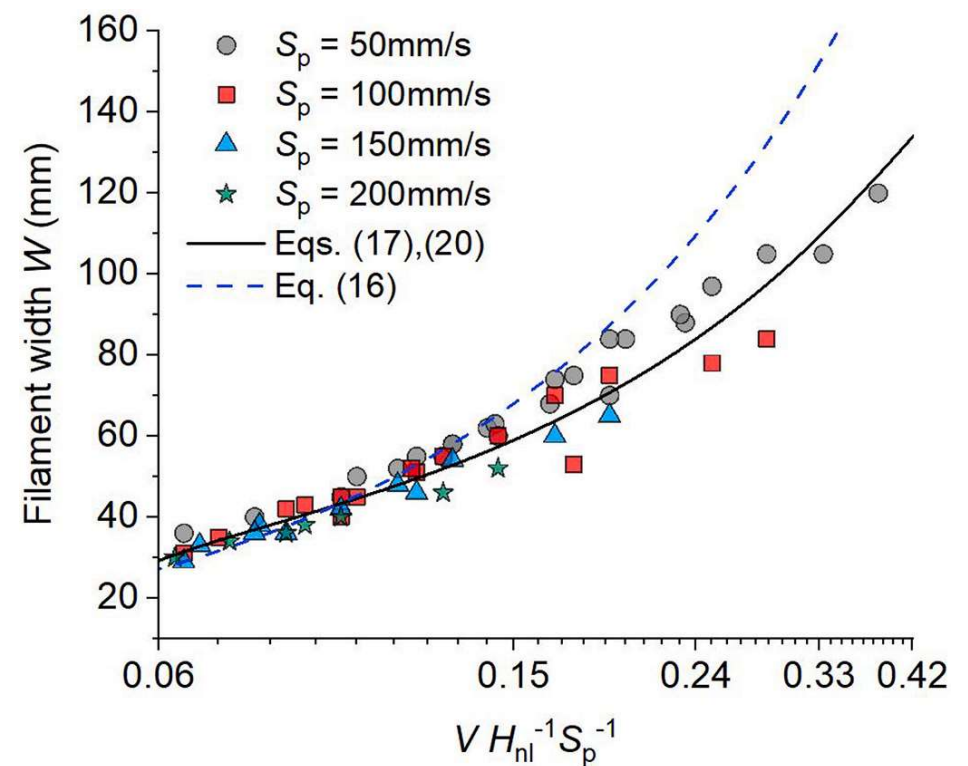


Fig. 20. Filament width as a function of print parameters with a nozzle outlet diameter of 24 mm.

$$\kappa = 0.7 - 1.6 \frac{t_2}{t_1} \quad \left( 0.1 \leq \frac{t_2}{t_1} \leq 0.7 \right) \quad (20)$$

This finding confirms that  $\kappa$  is dependent on the proportion between  $t_1$  and  $t_2$ , regardless of printing parameters. These constants (i.e., 0.7 and 1.6) could be related to the rheological parameters of printed concrete. On the one hand, Nguyen et al. [62] pointed out that, for a L-box concrete test, the final shape of fresh concrete flowing from the L-box is associated with the yield stress and viscosity of concrete and the flow's kinetic energy (related to the lifting speed of the tester gate). This lifting speed can be equivalent to print parameters in the 3D printing process. On the other hand, using a computational fluid dynamics (CFD) method, Wolfs et al. [63] showed that these rheological parameters of concrete affect the geometry control of 3D printed filaments. Further studies will be required to establish the relationships between concrete rheological parameters and these constants mentioned in Eq. (20).

Fig. 20 compares experimental data with calculational results by Eqs. (16), (17) and (20). It can be seen that the optimized model presents a good correlation with experimental data. This also confirms that once the rheological behaviors of concrete are given, the printing quality can be pre-assessed by evaluating the  $\kappa$  calculated from these parameters,

including extrusion velocity, printing speed, nozzle outlet diameter, and printing height. It is worth mentioning that according to Eq. (1), the extrusion velocity depends on the cone angle, the entrance and outlet diameters of this nozzle and the extrusion resistance. Thus, the filament dimensions can be anticipated in accordance with these nozzle dimensions, print parameters and  $\kappa$ .

Finally, the correlation between print parameters and nozzle outlet diameter can be written by:

$$W_m = \frac{\left[ \pi \left( \frac{N_D}{2} \right)^2 \frac{V}{H_n S_p} + \kappa N_D \right]}{(1 + \kappa)}$$

and

$$\kappa = a - b \frac{H_n S_p}{N_D V} \quad \left( 0.1 \leq \frac{H_n S_p}{N_D V} \leq 0.7 \right) \quad (21)$$

where  $a$  and  $b$  are constant. This model can be used to anticipate filament dimensions and potentially help control the print process more precisely.

## 6. Conclusion

This study presents a methodology for optimizing a printhead theoretically to reduce the extrusion resistance in a round nozzle. This printhead was customized and used to investigate the effect of print parameters and nozzle dimensions on printing quality. The following conclusions are drawn.

- Based on theoretical and experimental calibration, it is possible to develop a relationship between nozzle dimensions and print parameters, as presented in Equation (21). This relationship can be used as a basis for the design of nozzles and the selection of print parameters to achieve good-quality printing.
- To achieve good dimension consistency and free of surface defects, the nozzle lift height should be equal to the layer thickness. Furthermore, these print parameters need to be controlled within certain limitations.
- The printing speed dominates the layer thickness that can be printed. The decrease in printing speed will increase the printable limits of layer thickness.
- Regardless of printing speeds, the layer width increased linearly with increasing extrusion velocity.
- The length and cone angle of the round nozzle affects the extrusion resistance. Regarding fixed nozzle dimensions, lowering the extrusion velocity and the yield stress of printed concrete can reduce the extrusion resistance in the nozzle.

## Declaration of competing interest

The authors declare that they have no known competing financial interests or personal relationships that could have appeared to influence the work reported in this paper.

## Data availability

Data will be made available on request.

## Acknowledgements

The authors gratefully acknowledge the assistance by Guoyou Li from the technical centre of China State Construction Engineering Corporation. The authors also gratefully acknowledge the financial support from the Australian Research Council Grant DP170103521 and LE170100168 for the research work reported in this paper.

## References

- [1] R.A. Buswell, W.R. Leal de Silva, S.Z. Jones, J. Dirrenberger, 3D printing using concrete extrusion: a roadmap for research, *Cement Concr. Res.* 112 (2018) 37–49, <https://doi.org/10.1016/j.cemconres.2018.05.006>.
- [2] D. Asprone, C. Menna, F.P. Bos, T.A.M. Salet, J. Mata-Falcón, W. Kaufmann, Rethinking reinforcement for digital fabrication with concrete, *Cement Concr. Res.* 112 (2018) 111–121, <https://doi.org/10.1016/j.cemconres.2018.05.020>.
- [3] D. Lowke, E. Dini, A. Perrot, D. Weger, C. Gehlen, B. Dillenburger, Particle-bed 3D printing in concrete construction – possibilities and challenges, *Cement Concr. Res.* 112 (2018) 50–65, <https://doi.org/10.1016/j.cemconres.2018.05.018>.
- [4] T. Marchment, J. Sanjayan, Mesh reinforcing method for 3D concrete printing, *Autom. ConStruct.* 109 (2020), <https://doi.org/10.1016/j.autcon.2019.102992>.
- [5] M.K. Mohan, A.V. Rahul, G. De Schutter, K. Van Tittelboom, Extrusion-based concrete 3D printing from a material perspective: a state-of-the-art review, *Cem. Concr. Compos.* 115 (2021), 103855, <https://doi.org/10.1016/j.cemconcomp.2020.103855>.
- [6] B. Khoshnevis, Automated construction by contour crafting - related robotics and information technologies, *Autom. ConStruct.* 13 (2004) 5–19, <https://doi.org/10.1016/j.autcon.2003.08.012>.
- [7] S. Yu, H. Du, J. Sanjayan, Aggregate-bed 3D concrete printing with cement paste binder, *Cement Concr. Res.* 136 (2020), 106169, <https://doi.org/10.1016/j.cemconres.2020.106169>.
- [8] E. Lloret-Fritsch, T. Wangler, L. Gebhard, J. Mata-Falcón, S. Mantellato, F. Scotti, J. Burger, A. Szabo, N. Ruffray, L. Reiter, F. Boscaro, W. Kaufmann, M. Kohler, F. Gramazio, R. Flatt, From smart dynamic casting to a growing family of digital casting systems, *Cement Concr. Res.* 134 (2020), <https://doi.org/10.1016/j.cemconres.2020.106071>.
- [9] E. Lloret, A.R. Shahab, M. Linus, R.J. Flatt, F. Gramazio, M. Kohler, S. Langenberg, Complex concrete structures: merging existing casting techniques with digital fabrication, *CAD Comput. Aided Des.* 60 (2015) 40–49, <https://doi.org/10.1016/j.cad.2014.02.011>.
- [10] S. Neudecker, C. Bruns, R. Gerbers, J. Heyn, F. Dietrich, K. Dröder, A. Raatz, H. Kloft, A new robotic spray technology for generative manufacturing of complex concrete structures without formwork, *Procedia CIRP* 43 (2016) 333–338, <https://doi.org/10.1016/j.procir.2016.02.107>.
- [11] H. Kloft, H.W. Krauss, N. Hack, E. Herrmann, S. Neudecker, P.A. Varady, D. Lowke, Influence of process parameters on the interlayer bond strength of concrete elements additive manufactured by Shotcrete 3D Printing (SC3DP), *Cem. Concr. Res.* 134 (2020), 106078, <https://doi.org/10.1016/j.cemconres.2020.106078>.
- [12] I. Dressler, N. Freund, D. Lowke, The effect of accelerator dosage on fresh concrete properties and on interlayer strength in shotcrete 3D printing, *Materials* 13 (2020), <https://doi.org/10.3390/ma13020374>.
- [13] F.P. Bos, C. Menna, M. Pradena, E. Kreiger, W.R.L. da Silva, A.U. Rehman, D. Weger, R.J.M. Wolfs, Y. Zhang, L. Ferrara, V. Mechtkerine, The realities of additively manufactured concrete structures in practice, *Cement Concr. Res.* 156 (2022), 106746, <https://doi.org/10.1016/j.cemconres.2022.106746>.
- [14] A.V. Rahul, M. Santhanam, H. Meena, Z. Ghani, 3D printable concrete: mixture design and test methods, *Cem. Concr. Compos.* 97 (2019) 13–23, <https://doi.org/10.1016/j.cemconcomp.2018.12.014>.
- [15] D. Marchon, S. Kawashima, H. Bessaias-Bey, S. Mantellato, S. Ng, Hydration and rheology control of concrete for digital fabrication: potential admixtures and cement chemistry, *Cement Concr. Res.* 112 (2018) 96–110, <https://doi.org/10.1016/j.cemconres.2018.05.014>.
- [16] M. Chen, L. Li, Y. Zheng, P. Zhao, L. Lu, X. Cheng, Rheological and mechanical properties of admixtures modified 3D printing sulphoaluminate cementitious materials, *Construct. Build. Mater.* 189 (2018) 601–611, <https://doi.org/10.1016/j.conbuildmat.2018.09.037>.
- [17] N. Roussel, Rheological requirements for printable concretes, *Cement Concr. Res.* 112 (2018) 76–85, <https://doi.org/10.1016/j.cemconres.2018.04.005>.
- [18] R. Jayathilakage, J. Sanjayan, P. Rajeev, Direct shear test for the assessment of rheological parameters of concrete for 3D printing applications, *Mater. Struct. Constr.* 52 (2019) 1–13, <https://doi.org/10.1617/s11527-019-1322-4>.
- [19] B. Panda, C. Unluer, M.J. Tan, Investigation of the rheology and strength of geopolymer mixtures for extrusion-based 3D printing, *Cem. Concr. Compos.* 94 (2018) 307–314, <https://doi.org/10.1016/j.cemconcomp.2018.10.002>.
- [20] R.J.M. Wolfs, F.P. Bos, T.A.M. Salet, Early age mechanical behaviour of 3D printed concrete: numerical modelling and experimental testing, *Cement Concr. Res.* 106 (2018) 103–116, <https://doi.org/10.1016/j.cemconres.2018.02.001>.
- [21] T.T. Le, S.A. Austin, S. Lim, R.A. Buswell, R. Law, A.G.F. Gibb, T. Thorpe, Hardened properties of high-performance printing concrete, *Cement Concr. Res.* 42 (2012) 558–566, <https://doi.org/10.1016/j.cemconres.2011.12.003>.
- [22] R.J.M. Wolfs, F.P. Bos, T.A.M. Salet, Hardened properties of 3D printed concrete: the influence of process parameters on interlayer adhesion, *Cement Concr. Res.* 119 (2019), <https://doi.org/10.1016/j.cemconres.2019.02.017>.
- [23] B. Zareyan, B. Khoshnevis, Effects of interlocking on interlayer adhesion and strength of structures in 3D printing of concrete, *Autom. ConStruct.* 83 (2017) 212–221, <https://doi.org/10.1016/j.autcon.2017.08.019>.
- [24] J.G. Sanjayan, B. Nematollahi, M. Xia, T. Marchment, Effect of surface moisture on inter-layer strength of 3D printed concrete, *Construct. Build. Mater.* 172 (2018) 468–475, <https://doi.org/10.1016/j.conbuildmat.2018.03.232>.
- [25] M.K. Mohan, A.V. Rahul, K. Van Tittelboom, G. De Schutter, Rheological and pumping behaviour of 3D printable cementitious materials with varying aggregate content, *Cement Concr. Res.* 139 (2021), 106258, <https://doi.org/10.1016/j.cemconres.2020.106258>.

- [26] B. Dreith, ICON and Lake Flato Build 3D-Printed House Zero in Austin, Dezeen, 2022. <https://www.dezeen.com/2022/03/04/icon-lake-flato-3d-printed-house-zero-austin/>.
- [27] M.C. Tim Agne, 3D Printer Builds Most of New Habitat for Humanity Home in Tempe, Fronteras, 2021. <https://fronterasdesk.org/content/1690185/3d-printer-builds-most-new-habitat-humanity-home-tempe>.
- [28] 3DCP & Saga Space Architects, 3D PRINTED TINY HOUSE, 2022. <https://www.cpt-worldwide.com/projects-85/issue-135/3d-printed-tiny-house-2109>.
- [29] Serendix, Japanese Company Serendix Is 3D-Printing Houses in Less than 24 Hours, Designboom, 2022. <https://www.designboom.com/technology/serendix-3d-printed-house-24-hours-03-14-2022/>.
- [30] PERI, Germany's First Printed House Officially Openend, 2021. <https://www.peri.com/en/company/press-releases/germanys-first-printed-house-officially-openend.html>.
- [31] Project Milestone 3Dprintedhouse, 3Dprintedhouse, 2022. <https://www.3dprintedhouse.nl/en/project-info/project-milestone/>.
- [32] A. Kazemian, X. Yuan, E. Cochran, B. Khoshnevis, Cementitious materials for construction-scale 3D printing : laboratory testing of fresh printing mixture, *Construct. Build. Mater.* 145 (2017) 639–647, <https://doi.org/10.1016/j.conbuildmat.2017.04.015>.
- [33] S.C. Paul, Y.W.D. Tay, B. Panda, M.J. Tan, Fresh and hardened properties of 3D printable cementitious materials for building and construction, *Arch. Civ. Mech. Eng.* 18 (2018) 311–319, <https://doi.org/10.1016/j.acme.2017.02.008>.
- [34] A. Kazemian, X. Yuan, E. Cochran, B. Khoshnevis, Cementitious materials for construction-scale 3D printing: laboratory testing of fresh printing mixture, *Construct. Build. Mater.* 145 (2017) 639–647, <https://doi.org/10.1016/j.conbuildmat.2017.04.015>.
- [35] H. Kwon, S. Bukkapatnam, B. Khoshnevis, J. Saito, Effects of orifice shape in contour crafting of ceramic materials, *Rapid Prototyp. J.* 8 (2002) 147–160, <https://doi.org/10.1108/13552540210430988>.
- [36] ArchDaily, 3D Printing Fuses Thai Craftsmanship to Create Habitable Concrete Structures, 2018. <https://www.archdaily.com/887403/3d-printing-fuses-thai-craftsmanship-to-create-habitable-concrete-structures>.
- [37] 3dnatives, XtreeE Prints Concrete 3D Printed Benches with Complex Patterns, 2018. <https://www.3dnatives.com/en/xtreee-concrete-bench-3d-printed-benches-patterns-140920184/>.
- [38] T.T. Le, S.A. Austin, S. Lim, R.A. Buswell, A.G.F. Gibb, T. Thorpe, Mix design and fresh properties for high-performance printing concrete, *Mater. Struct.* 45 (2012) 1221–1232, <https://doi.org/10.1617/s11527-012-9828-z>.
- [39] D. Asprone, F. Auricchio, C. Menna, V. Mercuri, 3D printing of reinforced concrete elements: technology and design approach, *Construct. Build. Mater.* 165 (2018) 218–231, <https://doi.org/10.1016/j.conbuildmat.2018.01.018>.
- [40] B. Panda, S.C. Paul, N.A.N. Mohamed, Y.W.D. Tay, M.J. Tan, Measurement of tensile bond strength of 3D printed geopolymers mortar, *Meas. J. Int. Meas. Confed.* 113 (2018) 108–116, <https://doi.org/10.1016/j.measurement.2017.08.051>.
- [41] Y.W.D. Tay, M.Y. Li, M.J. Tan, Effect of printing parameters in 3D concrete printing: printing region and support structures, *J. Mater. Process. Technol.* 271 (2019) 261–270, <https://doi.org/10.1016/j.jmatprotec.2019.04.007>.
- [42] N. Roussel, A thixotropy model for fresh fluid concretes: theory, validation and applications, *Cement Concr. Res.* 36 (2006) 1797–1806, <https://doi.org/10.1016/j.cemconres.2006.05.025>.
- [43] R.A. Basterfield, C.J. Lawrence, M.J. Adams, On the interpretation of orifice extrusion data for viscoplastic materials, *Chem. Eng. Sci.* 60 (2005) 2599–2607, <https://doi.org/10.1016/j.ces.2004.12.019>.
- [44] H. Khelifi, A. Perrot, T. Lecompte, D. Rangeard, G. Ausias, Prediction of extrusion load and liquid phase filtration during ram extrusion of high solid volume fraction pastes, *Powder Technol.* 249 (2013) 258–268, <https://doi.org/10.1016/j.powtec.2013.08.023>.
- [45] A.H. Behravesh, E. Shakouri, A. Zolfaghari, M. Golzar, Theoretical and experimental study on die pressure prediction in extrusion of wood-plastic composite, *J. Compos. Mater.* 44 (2010) 1293–1304, <https://doi.org/10.1177/0021998309352703>.
- [46] A. Perrot, Y. Mélinge, D. Rangeard, F. Micaelli, P. Estellé, C. Lanos, Use of ram extruder as a combined rheo-tribometer to study the behaviour of high yield stress fluids at low strain rate, *Rheol. Acta* 51 (2012) 743–754, <https://doi.org/10.1007/s00397-012-0638-6>.
- [47] S. Chaves Figueiredo, C. Romero Rodríguez, Z.Y. Ahmed, D.H. Bos, Y. Xu, T. M. Salet, O. Çopuroğlu, E. Schlangen, F.P. Bos, An approach to develop printable strain hardening cementitious composites, *Mater. Des.* 169 (2019), 107651, <https://doi.org/10.1016/j.matdes.2019.107651>.
- [48] A. Perrot, C. Lanos, P. Estellé, Y. Melinge, Ram extrusion force for a frictional plastic material: model prediction and application to cement paste, *Rheol. Acta* 45 (2006) 457–467, <https://doi.org/10.1007/s00397-005-0074-y>.
- [49] X. Zhou, Z. Li, M. Fan, H. Chen, Rheology of semi-solid fresh cement pastes and mortars in orifice extrusion, *Cem. Concr. Compos.* 37 (2013) 304–311, <https://doi.org/10.1016/j.cemconcomp.2013.01.004>.
- [50] R. O'Neill, H.O. McCarthy, E. Cunningham, E. Montufar, M.P. Ginebra, D.I. Wilson, A. Lennon, N. Dunne, Extent and mechanism of phase separation during the extrusion of calcium phosphate pastes, *J. Mater. Sci. Mater. Med.* 27 (2016) 1–13, <https://doi.org/10.1007/s10856-015-5615-z>.
- [51] J.J. Benbow, S.H. Jazayeri, J. Bridgwater, The flow of pastes through dies of complicated geometry, *Powder Technol.* 65 (1991) 393–401, [https://doi.org/10.1016/0032-5910\(91\)80201-S](https://doi.org/10.1016/0032-5910(91)80201-S).
- [52] G. Lu, K. Wang, Investigation into yield behavior of fresh cement paste: model and experiment, *ACI Mater. J.* 107 (2010) 12–19.
- [53] BS EN 197-1, Cement - Part 1: Composition, Specifications and Conformity Criteria for Common Cements, Eur. Stand., 2011, p. 50.
- [54] Schleibinger, Schleibinger Testing Systems, 2020. [http://www.schleibinger.com/cmsimple/en/?Rheometers:Viskomat\\_XL\\_-Rheometer\\_for\\_Mortar\\_and\\_Fresh\\_Concrete](http://www.schleibinger.com/cmsimple/en/?Rheometers:Viskomat_XL_-Rheometer_for_Mortar_and_Fresh_Concrete).
- [55] N. Roussel, G. Ovarlez, S. Garrault, C. Brumaud, The origins of thixotropy of fresh cement pastes, *Cement Concr. Res.* 42 (2012) 148–157, <https://doi.org/10.1016/j.cemconres.2011.09.004>.
- [56] S. Hou, Z. Duan, J. Xiao, L. Li, Y. Bai, Effect of moisture condition and brick content in recycled coarse aggregate on rheological properties of fresh concrete, *J. Build. Eng.* 35 (2021), <https://doi.org/10.1016/j.jobe.2020.102075>.
- [57] J.T. Kolawole, R. Combrinck, W.P. Boshoff, Measuring the thixotropy of conventional concrete: the influence of viscosity modifying agent, superplasticiser and water, *Construct. Build. Mater.* 225 (2019) 853–867, <https://doi.org/10.1016/j.conbuildmat.2019.07.240>.
- [58] S. Ma, Y. Qian, S. Kawashima, Experimental and modeling study on the non-linear structural build-up of fresh cement pastes incorporating viscosity modifying admixtures, *Cement Concr. Res.* 108 (2018) 1–9, <https://doi.org/10.1016/j.cemconres.2018.02.022>.
- [59] D. Feys, J.E. Wallevik, A. Yahia, K.H. Khayat, O.H. Wallevik, Extension of the Reiner-Riwlin equation to determine modified Bingham parameters measured in coaxial cylinders rheometers, *Mater. Struct.* 46 (2013) 289–311, <https://doi.org/10.1617/s11527-012-9902-6>.
- [60] A.T.J. Domanti, J. Bridgwater, Surface fracture in axisymmetric paste extrusion: an experimental study, *Chem. Eng. Res. Des.* 78 (2000) 68–78, <https://doi.org/10.1205/026387600526898>.
- [61] H. Zhang, J. Wang, Y. Liu, X. Zhang, Z. Zhao, Effect of processing parameters on the printing quality of 3D printed composite cement-based materials, *Mater. Lett.* 308 (2022), 131271, <https://doi.org/10.1016/j.matlet.2021.131271>.
- [62] T.L.H. Nguyen, N. Roussel, P. Coussot, Correlation between L-box test and rheological parameters of a homogeneous yield stress fluid, *Cement Concr. Res.* 36 (2006) 1789–1796, <https://doi.org/10.1016/j.cemconres.2006.05.001>.
- [63] R.J.M. Wolfs, T.A.M. Salet, N. Roussel, Filament geometry control in extrusion-based additive manufacturing of concrete: the good, the bad and the ugly, *Cement Concr. Res.* 150 (2021), 106615, <https://doi.org/10.1016/j.cemconres.2021.106615>.